ADVANCED MATERIALS
www.advmat.de

Broadband THz Modulation via Solid-State Organic Electrochemical Devices

*Jonathan Scott, Atsutse Kludze, Megan Santamore, Christina J. Kousseff, Iain McCulloch, Yasaman Ghasempour, and Barry P. Rand**

The sub-Terahertz and Terahertz bands play a critical role in next-generation wireless communication and sensing technologies, thanks to the large amount of available bandwidth in this spectral regime. While long-wavelength (microwave to mm-Wave) and short-wavelength (near-infrared to ultraviolet) devices are well-established and studied, the sub-THz to THz regime remains relatively underexplored and underutilized. Traditional approaches used in the aforementioned spectral regions are more difficult to replicate in the THz band, leading to the need for the development of novel devices and structures that can manipulate THz radiation effectively. Herein a novel organic, solid-state electrochemical device is presented, capable of achieving modulation depths of over 90% from ≈500 nm of a conducting polymer that switches conductivity over a large dynamic range upon application of an electronically controllable external bias. The stability of such devices under long-term, repeated voltage switching, as well as continuous biasing at a single voltage, is also explored. Switching stabilities and long-term bias stabilities are achieved over two days for both use cases. Additionally, both depletion mode (always "ON") and accumulation mode (always "OFF") operation are demonstrated. These results suggest applications of organic electrochemical THz modulators in large area and flexible implementations.

1. Introduction

The ongoing push toward higher frequencies and the concomitant bandwidths required for next-generation communications systems, biomedical diagnostics, imaging and spectroscopic systems, and other technologies necessitate new paradigms of materials and devices. The ability to dynamically control the transmission of such frequencies is of critical need for modulation and reconfigurability of GHz to THz devices. Active THz modulators and switches capable of achieving large bandwidths are an ongoing area of research. Current technologies include metamaterials, optically and electrically gated semiconductor devices, as well as devices based on 2D materials such as graphene.[1–6] However, all such devices require specialized design and fabrication techniques, hindering ease of use, scalability, and integration into THz systems.

Conjugated polymer based electronic devices such as solar cells and light-emitting devices have showcased the diverse capabilities of this material class, with the added benefit of facile processing and fabrication.[7–9] One such area of active conjugated polymer research is in organic electrochemical transistors (OECTs) which have shown promise in emerging areas of bioelectronics.[10–13] The channel layer of such transistors consists of an organic mixed ionic-electronic conductor (OMIEC), the conductivity of which can be modulated by the application of a small external bias to an adjacent electrolyte, resulting in ionic injection into the bulk of the channel and consequent stabilization of charge transport in the channel. The DC conductivity change also has demonstrated effects in higher frequency regimes.[14–16] Traditional electrolytes in OECTs include aqueous ionic species such as NaCl diluted in water.[10] Recent advances in electrolyte materials include ionic liquids or solid-state electrolytes consisting of ionic species contained in a structured polymer network through which they can migrate.[17–19]

The modulation of material properties beyond DC conductivity based on redox chemistry is illustrated by the use of OMIECs in electrochromic devices (ECDs).[20–22] One of the most common OMIECs used in both OECTs and ECDs is a combination of poly(3,4-ethylenedioxythiophene) (PEDOT) and polystyrene sulfonate (PSS), or PEDOT:PSS. The PEDOT cation is an excellent

J. Scott, A. Kludze, M. Santamore, I. McCulloch, Y. Ghasempour, B. P. Rand
Department of Electrical & Computer Engineering
Princeton University
Princeton, NJ 08544, USA
E-mail: brand@princeton.edu
C. J. Kousseff
Department of Chemistry
University of Oxford
Oxford OX1 3TA, UK
I. McCulloch, B. P. Rand
Andlinger Center for Energy & The Environment
Princeton University
Princeton, NJ 08544, USA

The ORCID identification number(s) for the author(s) of this article can be found under https://doi.org/10.1002/adma.202415828

DOI: 10.1002/adma.202415828

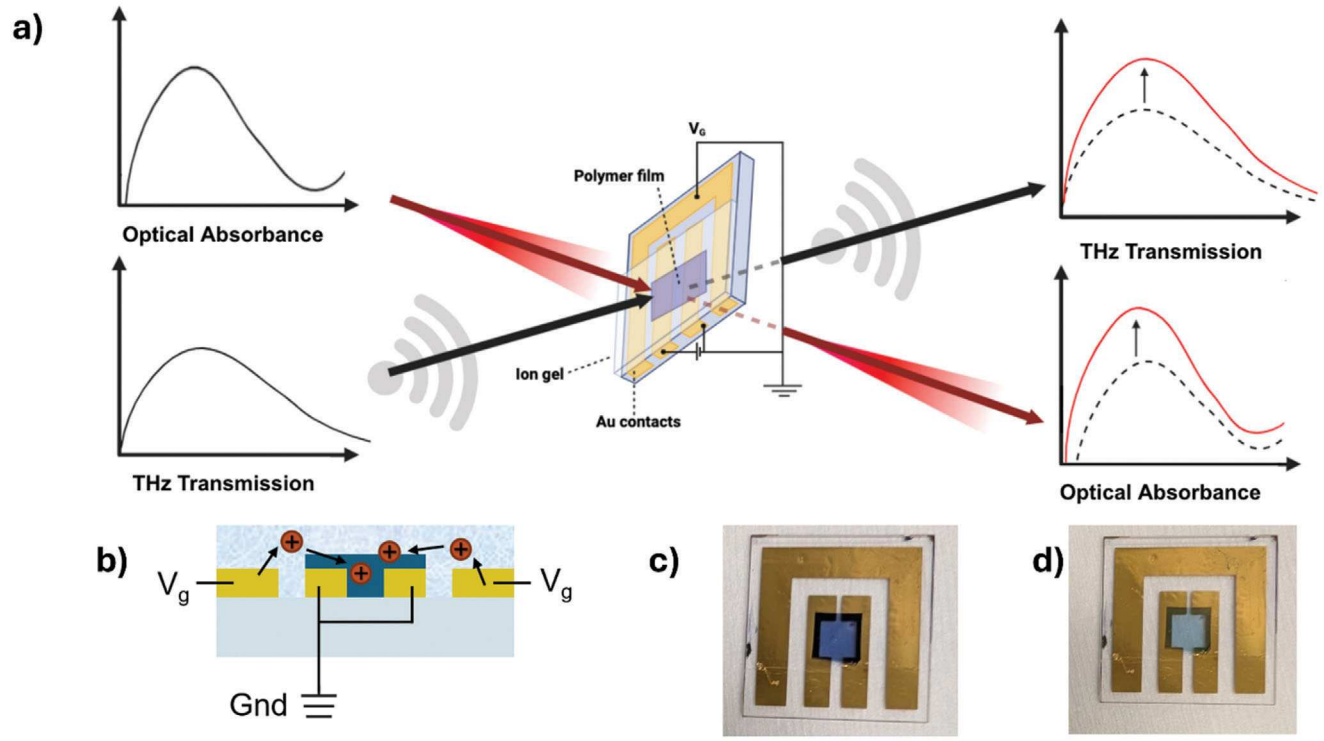

Figure 1. a) Diagram illustrating concurrent DC conductivity, THz, and UV–Vis–NIR optical measurements b) Schematic of a depletion mode OECT; cations from the electrolyte are injected into the channel, compensating anions that stabilize holes in the channel, leading to decreased conductivity c) Example accumulation mode device. The central area (0.6 x 0.6 cm) is the active area through which THz and optical radiation are passed and the change in transmission is measured. DC conductivity is measured across the two inner contacts. d) Doped accumulation mode device after applied gate voltage, showing electrochromic effect and uniformity of channel doping across the interior area.

ionic and electronic conductor, with the PSS anion acting as a counterion to stabilize holes in the p-type PEDOT phases. Upon application of a positive bias to an adjacent electrolyte, cations migrate into the PEDOT:PSS channel layer, compensating the PSS anions, decreasing hole concentration and thus conductivity. This also results in a change in the color of the PEDOT:PSS channel due to the differing absorption characteristics of the neutral and charged PEDOT species, known as electrochromic switching. Since the device is considered conductive or "ON" without an external bias, its operation is considered to be in depletion mode. Similar effects can occur in accumulation mode devices, where anions migrate into the bulk of a non-conductive polymer backbone under bias, stabilizing holes in the backbone and increasing conductivity in the channel. Such processes are reversible upon removal of the bias, as ions are allowed to migrate back into the electrolyte.

Drawing inspiration from the conductivity modulation capability of OECTs and optical switching capabilities of electrochromic devices, we present herein a device structure capable of modulating incident THz radiation upon application of an external voltage bias. We are able to achieve significant transmission modulation over 87.5% (or 9 dB) from just a single layer of a mixed ionic-electronic conductive material. The device consists of an OMIEC channel that is dynamically "de-doped" in response to an external bias applied to an ion gel electrolyte. We demonstrate operation in both depletion and accumulation mode, switching between a conductive – THz damping – state and a non-conductive – THz transmissive – state. We also demonstrate the connection of this behavior to optical switching, verifying the electrochromic behavior of the devices and their multispectral character across DC, THz, and optical regimes.

2. Results and Discussion

Figure 1 shows schematics of the measurement setup for concurrent, in operando measurement of DC conductivity, THz, and ultraviolet–visible–near–infrared (UV–vis–NIR) optical switching. Upon application of a gate voltage (V_g), mobile ions in the electrolyte enter the polymer channel layer, modulating the conductivity of the film. When a concurrent bias is applied to the two inner contacts transverse to the gate (V_{ds}) as displayed in Figure 1a, a current is induced to monitor conductivity, akin to traditional OECT operation. The broadband THz radiation is measured normal to the DC channel conduction, while the visible light probed at 632 nm is measured through a small spot size ($\lesssim$1 mm) on the channel material at a 45° angle. Figure 1b shows an example depletion mode OECT, with a positive gate bias causing the reduction of the PEDOT phases to the neutral state due to PSS anions pairing with injected cations, leading to increased THz transmission. An accumulation mode device with a poly(2-(4,4′-bis(2-methoxyethoxy)-5′-methyl-[2,2′-bithiophen]-5-yl)-5-methylthieno[3,2-b]thiophene) pgBTTT channel layer operates by injection of anions into the thin film, leading to the stabilization of holes along the backbone.[23,24] For our

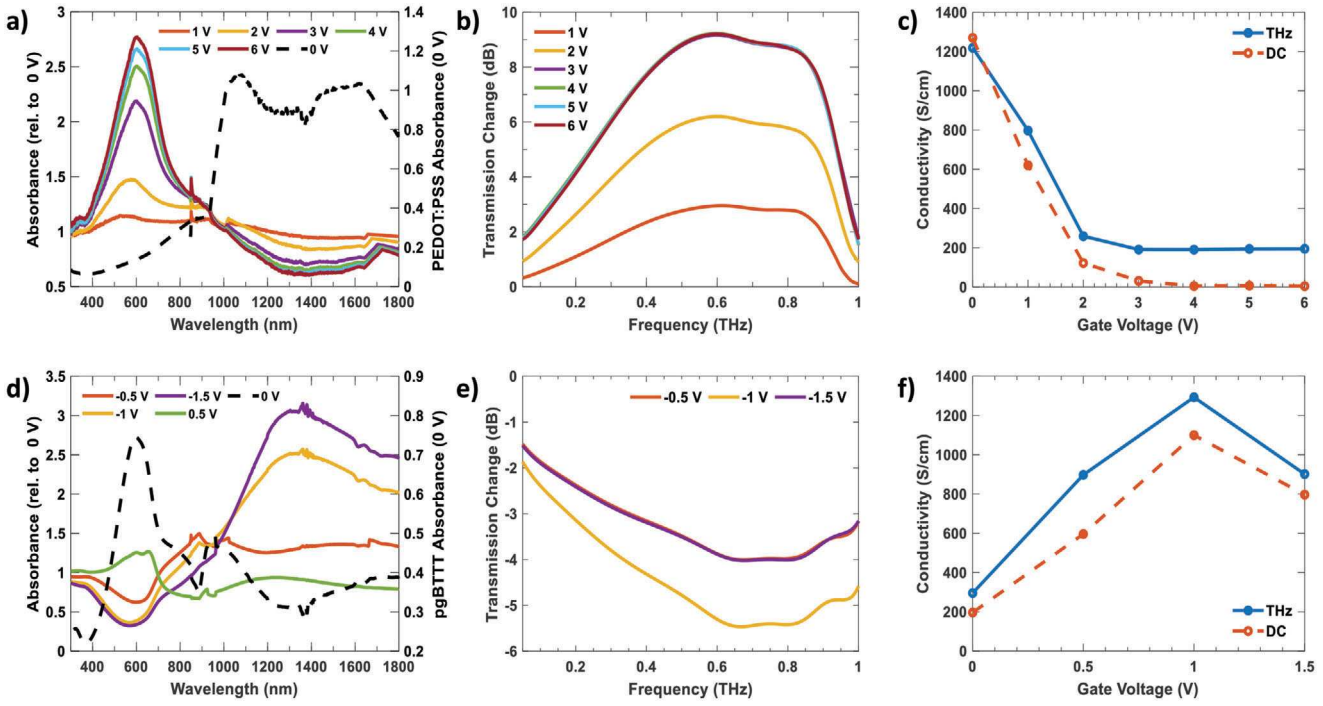

Figure 2. Optical, THz, and DC transmission/conductivity changes. a) Optical absorbance demonstrating PEDOT reduction upon application of a positive gate bias; b) THz transmission change, demonstrating over 9 dB (or 87.5%) modulation depth; c) Conductivity derived from THz or DC measurement; d) pgBTTT optical absorption data; e) demonstration of accumulation mode behavior in pgBTTT via THz damping upon reverse bias, achieving up to ≈5.5 dB or 72% modulation depth; f) calculation and comparison of THz/DC pgBTTT conductivity.

work, we chose this polymer for its increased transconductance, hole mobility, and specific capacitance compared to other glycolated polythiophenes.[23] In both cases, reversing the polarity of the applied gate voltage leads to the ejection of "counterions" in the bulk of the material, resetting the conductivity to near its initial value. Figure 1c,d presents images of a sample device. We utilize a three-terminal, bottom gate, and bottom contact device, where the gate is coplanar with the source and drain electrodes. For OECT operation, the gate bias is applied to the outer gold contact, while the DC (e.g., source to drain) conductivity is measured between the two inner contacts. For lone THz measurements, we ground the two inner contacts to the same potential to operate as a two-terminal device, with a gate voltage on the outer contact providing the impetus for ions to flow into the OMIEC.

Figure 2 presents static spectroelectrochemical, THz, and DC measurements of depletion and accumulation mode devices, respectively. As the channel of the depletion mode device becomes de-doped by injection of EIM cations into the bulk, the DC conductivity of the PEDOT:PSS channel drops as the PSS anion is compensated. This reaction is known to occur per the following equation:

$$PEDOT^{+}PSS^{-} + EIM^{+} + e^{-} \rightleftharpoons PEDOT^{0} + PSS^{-}EIM^{+} \quad (1)$$

This reaction occurs with a bipolaronic (or polaron pair) component as well, the nature of which is still under debate.[25,26] The structural changes that accompany the reduction of polaronic and bipolaronic PEDOT into neutral species are responsible for the change in conductivity and color of the channel layer. The neutral PEDOT phase is known to have an absorption peak at 660 nm, with the polaronic component at a wavelength of ≈1000 nm and an additional bipolaronic component at 1700 nm.[27] Additionally, treatment with an ionic liquid or a highly polar solvent can enhance the broad polaronic absorption peak at ≈1000 nm as compared to pristine PEDOT, which we see in our devices in comparison to pristine PEDOT.[28–30] We attribute the rapid extinction of our PEDOT absorption signal to detector changeover in our system, meaning we are not able to get highly accurate measurements in this near IR region. However, the broad absorption characteristics of the polaronic and bipolaronic states are clear in Figure 2a, with more importantly the clear change of the polaronic absorption in the IR and the neutral PEDOT absorption in the visible (≈660 nm) with increasing applied voltages (the colored lines, as compared to the 0 V absorption as the black dashed line). This demonstrates the expected electrochromic change upon reduction of PEDOT:PSS to its neutral state. We observe analogous behavior in the absorbance of the pgBTTT devices operating in accumulation mode in Figure 2d. The neutral phase absorption at ≈600 nm is suppressed upon application of a reverse bias to the device, with a corresponding absorbance increase in the NIR associated with polarons and increased electrical conductivity. The absorbance of the ion gels themselves in both the UV–Vis–NIR and THz are presented in Figure S6 (Supporting Information), with negligible contribution to the overall absorbance.

In conjunction with the UV–Vis–NIR absorption changes induced by V_g, the THz transmission change is demonstrated in

Figure 2b,e. Here we display the total transmission change at each frequency:

$$T(\omega)_{dB} = 10\log_{10}\frac{T_V(\omega)}{T_{0V}(\omega)} \quad (2)$$

where T_V is the transmission of the device at a given frequency and voltage, and $T_{0\ V}$ is the transmission of the same device at the same frequency at 0 V bias. In Figure S3 (Supporting Information), we demonstrate the correlated linear transmission rate, as well as the modulation depth versus frequency, found by taking the percent change of the linear transmission rate, $T(\omega) = \frac{T_V(\omega)}{T_{0V}(\omega)}$. The increase in THz transmission of the PEDOT:PSS films is illustrative of depletion mode behavior, while the decrease in the pgBTTT films demonstrates accumulation mode behavior. Thus, both modes of operation are available for THz modulators, allowing for future application of complementary logic/operation. We posit that the volumetric doping and de-doping of OMIEC films (as opposed to the thin inversion layers created in organic or inorganic field effect transistors), combined with the high conductivity shifts achievable in OMIECs, allow for strong incident THz modulation as displayed here. Bulk de-doping in an OMIEC film means a larger interaction volume with incident radiation and strong attenuation of THz radiation – even though the absolute conductivity of the OMIEC may be less than that of other materials traditionally used for THz modulation. Spectral changes in a thinner film of a depletion mode device can be seen in Figure S4 (Supporting Information) to support this assessment. The static optical and THz measurements show increasing modulation with increasing voltage for PEDOT:PSS, a phenomenon verified in the DC conductivity changes discussed below. However, we note that the pgBTTT films appear to be less stable under higher biases, as demonstrated by the decrease of THz transmission when compared to 1 V.

In Figure 2c,f, we demonstrate close correlation between the conductivity derived from the change in THz transmission with measured DC conductivity, confirming that charge carriers are responsible for the THz damping. In the absence of lattice contributions due to vibrational modes that often exist in the THz regime, the transmission of a highly conductive thin film can be found via the simple, closed-form expression:[31,32]

$$|T\ (\omega)| = \left|\frac{2}{2 + id\sigma Z_0}\right| \quad (3)$$

where T is the ratio of the transmitted THz power to the incident THz power, ω is the frequency, d is the thickness of the semiconducting material, σ its conductivity, and Z_0 is the characteristic impedance of free space, 377 Ω. For our purposes, we utilize the average of the conductivity values versus frequency (as displayed in Figure S9, Supporting Information) across the chosen flatband regions determined from Figures 2b,e. This equation holds for films of negligible optical thickness as used for our channel layers at the operating frequencies. Further, the DC conductivity of a semiconducting thin film is simply derived from the equation:

$$R = \rho\frac{L}{A} \quad (4)$$

where $\rho = 1/\sigma$ is the DC resistivity, L is the channel length, and A is the cross-sectional area (e.g., the product of the film thickness and the channel width). Figure 2c,f shows the correlation in the behavior of the THz and DC conductivity calculated from Equations (1) and (2) for both depletion and accumulation mode THz modulators. We attribute the small discrepancy in the THz versus DC measurements to the contact and parasitic resistance of the measurement setup. In summary, we show the close correlation of switching behavior across all three spectral domains, verifying the broadband and characteristic multispectral response of the devices.

The operation and behavior of depletion mode devices are presented in **Figures 3** and 4. We focus here on the multispectral, continuous switching of devices as the long-term stability under extended operation. Figure 3 demonstrates the close correlation of the DC conductivity, THz, and visible absorption (at 632 nm) under differing input square wave gate voltages, all with 60 s periods and 50% duty cycle (i.e., 30 s ON/OFF durations). The real-time modulation of the integrated THz power was measured by capturing single 700 ps waveforms output by the system and analyzing their spectral content as described in Methods. Exponential fits to the signal decay curves (Figure S5, Supporting Information) demonstrate a time constant on the order of 5 s, with greater dynamic range achievable with longer switching times. In order to ensure a complete saturation of the response and to achieve the highest dynamic range, this switching protocol was selected in order to balance speed and stability. The reverse bias applied during the square wave was −1 V for all devices and was used to eject EIM cations from the PEDOT:PSS film and achieve faster recovery times. We chose the flatband response of the system demonstrated in Figure 1b,e from 500 to 900 GHz as our integration region for calculating the total THz power. We observe switchable absorption at voltages as low as 1 V, with an increasing trend in dynamic range at higher voltages. Additionally, all voltages at or above 1.5 V demonstrate the capability of ≥6 dB switchable absorption over 10 min.

The simultaneous switching behavior discussed above also illustrates a key issue in the stability of these devices, namely the decrease in dynamic range of the THz transmission modulation in certain devices (devices at 3–5 V, specifically, in Figure 3) over 10 min, which is also demonstrated in the long-term measurements in Figure 4a,b. This is demonstrative of the key source of instability in the devices, a steady decrease in conductivity of the PEDOT:PSS films under repeated switching. In PEDOT:PSS, the PSS anion exists in the film to enhance solubility as well as provide a counterion to the PEDOT phases so that holes are stabilized along the backbone. However, the PSS anion itself is insulating, reducing the bulk conductivity of the channel material. The addition of a polar solvent (such as DMSO in our devices) greatly enhances the conductivity of the bulk material by reordering the morphology of the films such that longer, more aggregated PEDOT phases/crystallites exist, thus enhancing charge transport.[33–36] We posit that the repeated injection and ejection of cations into the PEDOT:PSS films, their repeated reduction and oxidation, as well as the associated swelling and contraction of the films, leads to their degradation over time. For example, the uptake of water in channel materials in OECTs and the resulting swelling of the films is a well-known phenomenon.[34–38]

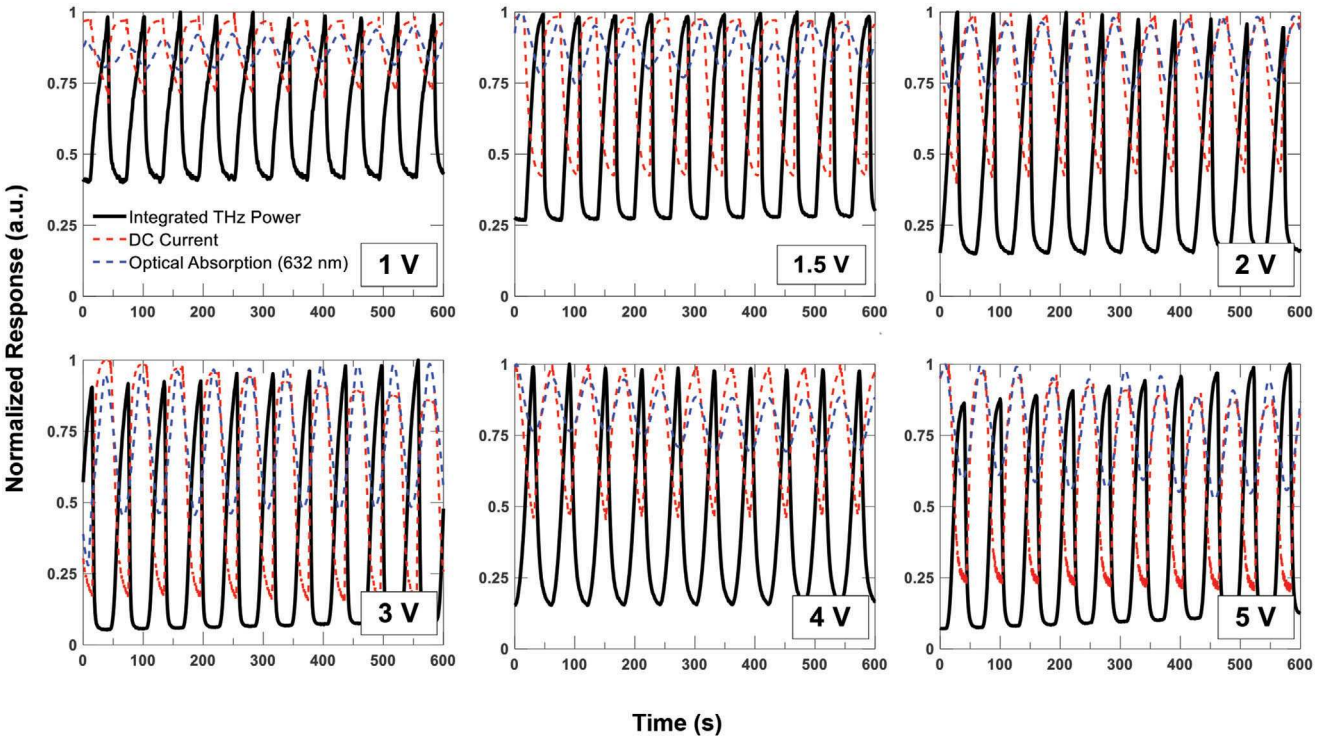

Figure 3. Depletion mode devices. Concurrent switching compared between DC, THz, and optical measurements. The THz signal is monitored across 400 GHz, while the optical transmission change is taken at 632 nm. All signals are normalized to their max response in the time range in order to display on the same axes.

If the morphology reverts to a more even distribution of PEDOT and PSS phases, the conductivity of the material overall would decay as observed in our long-term stability measurements. These lower conductivity films in turn reduce the dynamic range in the THz modulators. We note that the decay mechanism of our films is indicative of PEDOT:PSS becoming more insulating under repeated switching, with the final conductivity value similar to that of PEDOT:PSS films without DMSO treatment. We study this further by conducting extended device operations over two days to investigate the long-term stability under constant switching as well as constant bias. Figure 4a shows the THz power over longer time periods for three representative voltages, $V_g = 1$, 3, and 5 V, under continuous switching. There is a clear trend in THz transmission increasing over time, meaning a decrease in the overall conductivity of the film. This manifests as a decreased ability of the film to switch to a THz damping state with time, leading to a decreased dynamic range.

In order to assess long-term stability, we defined an upper and lower envelope signal (corresponding to the base, THz attenuating state, and the THz transmissive state achieved during cation injection) of the THz power over time and take the difference of these envelopes in a dB scale. We define two critical stability thresholds: the 6 and 3 dB points corresponding to 75% and 50% modulation depth respectively. Figure 4b shows the resulting lifetimes for each device at different voltages. The device biased at 3 V exhibits a 3 dB threshold of ≈20 h. We attribute this voltage being the most stable to the saturation of the THz response at 3 V evident in Figure 1b. In this scenario, 3 V achieves the maximum dynamic range in the device within its electrochemical stability window. There are myriad factors that determine the total THz absorption in both the attenuating and transmissive states that are challenging to rigorously control for, including the relationships between bias and total absorption, bias and rise times, the ability to completely recover from a doped state (e.g., fully eject ions from the film), and much more, that merit further study. However, a quick glance at the 3 V plot shows it appears to reside at a critical point of the slopes of the upper and lower envelopes, implying that the total difference between the doped and undoped states and their corresponding conductivities are well-matched, "balancing" each other well to achieve long-term stability. However, an increased voltage can provide additional dynamic range at the expense of stability, with 6 dB switchable absorption being possible for ≈5 h at 4 V. Additionally, we have observed that higher voltage operation (particularly 5 V and above) leads to a rapid decline in performance, with many devices failing in less than an hour, putting a limit on the operating voltages achievable in the devices.

We also see a key source of instability in Figure 4a for the switching devices, namely the reverse bias used to "reset" the conductivity of the films. The reverse bias on each switch does not typically fully recover the original transmission rate, i.e., the "doped transmission" trends higher with each switching period. As mentioned above, a delicate balance of factors is at play – in order to achieve switching within a 30 s window, the reverse bias is required to more quickly eject cations from the film. However, this corresponds to a decreasing conductivity over time. It is evident that there exist optimal biasing protocols that balance factors such as dynamic range, stability, and switching time, that

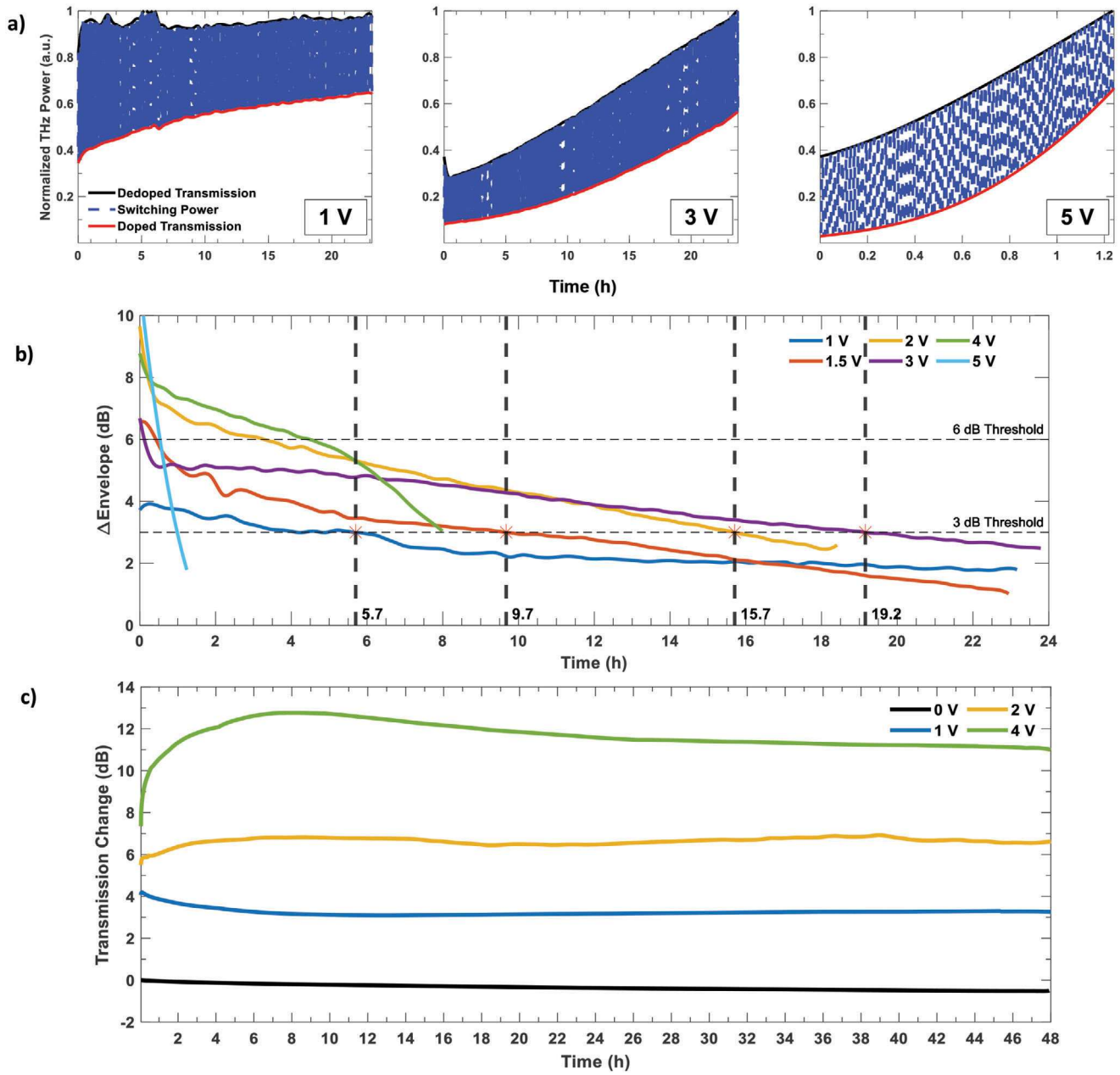

Figure 4. Depletion mode devices. a) Upper (black) and lower (red) envelope signals of the PEDOT:PSS THz transmission taken over long-term switching. The instantaneous normalized THz power is displayed in blue. b) The difference in the upper and lower envelopes (black and red lines in a) in dB, plotted vs time. Horizontal dashed lines show the 6 and 3 dB points for stability, where the difference in these envelopes falls below the threshold. 3 dB lifetimes for 1, 1.5, 2, and 3 V are displayed at the bottom of the vertical dashed lines. c) Transmission behavior of the PEDOT:PSS depletion mode devices under continuous bias.

should be explored further depending on the application. Further, it is possible that thinner layers could demonstrate faster switching times, as some OECT devices have demonstrated the ability to switch on µs timescales.[10] However, these are much thinner films with smaller active areas which would result in a very low dynamic range. A possible solution to this problem could be the layering of thinner channel layers, triggered to switch at the same time, or exploration of other volumetrically doped material systems that can be switched faster.

However, many applications in the areas of reconfigurable devices or sensors require operation under a constant bias for extended periods of time, where switching speeds are not as critical. For instance, THz biomedical imaging requires precise focal point control or non-invasive diagnostics and broadband spectra to achieve high resolution sensing.[39,40] Similarly, environmental sensing and climate studies rely on high spectral resolution to detect trace gases and aerosols under varying conditions.[41] Additionally, the use of the wideband THz

spectrum allows the facilitation of large scale dense wireless networks via frequency and space division multiplexing.[42] Communication systems demand dynamic beam shaping and frequency, particularly in mobile settings (we wish to note that in mobile communication links, the required switching speeds for beam shaping typically never exceed 10 ms).[43] The versatility required across these applications cannot be achieved in narrowband systems despite their fast switching capabilities. As such, our proposed organic electrochemical modulators fill this research gap by allowing wideband modulation capabilities, as well as compatibility with large area fabrication techniques and with a wider array of substrates, including flexible materials.

We probe this long-term reconfigurability in Figure 4c. Each bias point can be maintained for extended periods of time with little change, a promising feature for the long-term reconfigurability of devices. Figure 4c also demonstrates that significant change can be affected in the total THz absorption of the devices, with 4 V showing up to 95% absorption change when allowed to operate continuously at constant bias. We attribute this behavior to a more complete permeation of ions from the electrolyte throughout the entire bulk of the film, rather than a possibly "incomplete" ion injection that occurs when the bias is reversed before a more complete diffusion of ions can occur.

An important corollary of depletion mode device operation in OECTs is that of accumulation mode devices, where the channel material is normally insulating, or "OFF", and becomes conducting upon application of a bias. We demonstrate this accumulation mode capability in **Figure 5**, using the polymer pgBTTT as the active layer.[23,24] These devices operate with the gate electrode at a lower potential than the channel layer, implying the injection of anions into the polymer film as the mechanism for conductivity changes. Figure 5a illustrates the short-term switching behavior of the devices, while Figure 5b shows the long-term stability under continuous switching. Notably, pgBTTT shows enhanced stability when the applied bias is kept within an electrochemical stability window of the material, which we find to be roughly −1 V. Above this voltage, the devices rapidly degrade without the benefit of any clear additional dynamic range. However, when kept below this threshold the devices show impressive stability under continuous switching when compared to PEDOT:PSS. We demonstrate over two-days long continuous operation, nearly tripling that of the best depletion mode device. Hence the accumulation mode devices are capable of stable low-voltage operation, albeit within a narrower electrochemical stability window.

Finally, Figure 5c shows the long-term stability of the pgBTTT devices under continuous bias (i.e., no switching). We can see the rapid degradation of the −1.5 V device, corroborated by its instability seen in the continuous switching behavior. Notably, the continuous bias on the device appears to degrade its conductivity in the "ON" state even in the stable voltage regime, behavior that is not replicated in the PEDOT:PSS devices. The −1 V bias achieves up to 4.5 dB when initially applied, but over two days the conductivity slowly approaches the "OFF" state, indicative of an insulating channel layer. This suggests that accumulation mode devices based on pgBTTT would not be strong candidates for long-term reconfigurability, but would operate well for use cases where continuous switching (modulation, sensing, etc.) is required.

3. Conclusion

We have demonstrated the feasibility of organic electrochemical modulators in the THz regime and evaluated their multispectral switching behaviors (DC, THz, and optical), as well as their stability under continuous switching and constant bias. The devices show good agreement between all spectral regions observed, with corroborated conductivity calculations between DC and THz; spectroelectrochemistry measurements confirm the correspondence of the THz and visible spectrum electrochromism. Additionally, we have demonstrated both depletion and accumulation mode behavior, observing different stability behaviors. Depletion mode PEDOT:PSS devices show stability under repeated switching greater than 10 h, while the accumulation mode pgBTTT devices can operate for over 2 days under repeated switching. These time periods, corresponding to over 1000 and 3000 cycles respectively (as shown in Figure S2, Supporting Information), are on par with, and in some cases exceeding, comparable OECT devices in literature.[20,24,34,44–46] On the other hand, depletion mode devices show a high degree of stability over multiple days under a continuous bias, while their accumulation mode counterparts show degradation under similar conditions. Overall, this work indicates additional applications of conjugated polymer OMIECs and ECDs as electrochemical switches and modulators in the THz range, ranging from communication, reconfigurable waveguides, high bandwidth modulation, wireless sensing, bioelectronic devices, and more. We have achieved over 90% modulation depth from thin polymer films of a few hundred nanometers, and demonstrated their reversibility and reconfigurability. We anticipate that even greater modulation depths can readily be achieved with techniques that result in thicker films. Future work could explore increased modulation amplitude, causes of instability, and higher resolution patterning for wireless metasurfaces/metadevices, usage in flexible modulators, and many other potential applications.

4. Experimental Section

Ion Gel Preparation: The free-standing ion gels were prepared per ref. [47]. The protic ionic liquid 1-ethylimidazolium bis(trifluoromethylsulfonyl)imide, abbreviated [EIM][TFSI], was purchased from EvitaChem. The aprotic ionic liquid 1-ethyl-3-methylimidazolium bis(trifluoromethylsulfonyl)imide ([EMIM][TFSI]) and the copolymer poly(vinylidene fluoride-co-hexafluoropropylene) (p(VDF-HFP)) were purchased from Sigma–Aldrich. Both ionic liquids were dried in a vacuum oven at 70 °C for 24 h prior to mixing. The ion gel solution was prepared in a weight ratio of 17.6% ionic liquid, 4.4% p(VDF-HFP), and 78% acetone as solvent. The solutions were mixed overnight at 40 °C. The resulting solution was then drop cast onto glass slides, and left to dry in a vacuum oven for 24 h at 70 °C. The resulting ion gels were ≈100 µm thick and solid at room temperature. They were cut from glass slides and transferred onto the device substrate.

Device Fabrication: Clevios PH 1000 PEDOT:PSS was purchased from Heraeus. The PEDOT:PSS solution was mixed with 10% by wt. dimethyl sulfoxide (DMSO) as a conductivity promoter as per refs. [26,27] and was used in depletion mode devices. The polymer poly(2-(4,4′-bis(2-methoxyethoxy)-5′-methyl-[2,2′-bithiophen]-5-yl)-5-methylthieno[3,2-b]thiophene) (pgBTTT) used in enhancement mode devices was synthesized following past protocols per ref. [23] and dissolved in chloroform at a 10 mg mL^{-1} concentration. 100 nm Au contacts were patterned on glass using a shadow mask in a vacuum thermal evaporator, with a 3 nm Cr underlayer to promote adhesion. The choice of polarizable

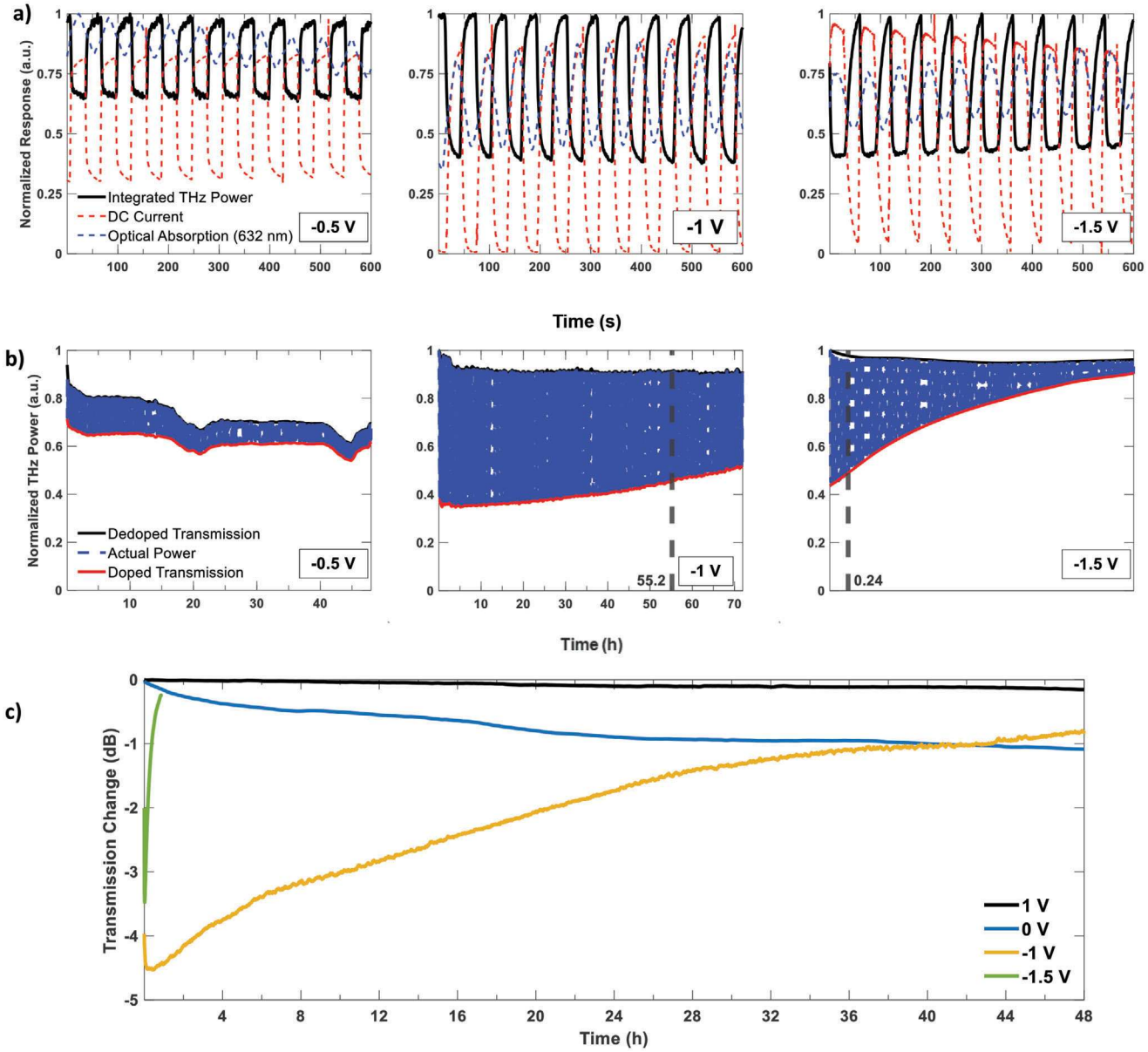

Figure 5. Accumulation Mode Devices. a) Multispectral switching behavior of pgBTTT-based accumulation mode devices b) Long-term switching behavior for accumulation mode devices. Note that the voltages are listed in reverse bias, meaning the channel layer is kept at a lower potential relative to the gate electrode. The reset pulse used for the −0.5 V device was 0.5 V, while that used for −1 and −1.5 was 1 V. c) Long-term biasing tests of accumulation mode device.

gate electrode was chosen for environmental and corrosion stability purposes, and the gate area was maximized within the device area in order to make the resulting gate-electrolyte capacitance as small as possible, thus minimizing the impact on gating efficiency.[48] The polymers were then spin-coated onto the gold contacts at 300 rpm (yielding ≈500 nm PEDOT:PSS and ≈250 nm pgBTTT thick films), and wet-patterned to remove material from unwanted areas. The resulting active area was 0.6 cm × 0.6 cm. Following annealing of the polymer at 120 °C for 30 min (PEDOT:PSS) and 100 °C for 30 min (pgBTTT), the ion gel was transferred onto the THz device by hand and cut to fit the active area of the device.

THz Measurements: The in situ THz time-domain spectroscopy (THz-TDS) data were collected using a TeraMetrix T-Ray 5000 from Luna Innovations. The system consists of a terahertz time-domain spectrometer (THz-TDS) with fiber-coupled photoconductive antennas. These two fiber-coupled photoconductive antennas are excited by fs-optical pulses, in which an optical delay line is used to retrieve the time-dependent THz electric field (measured in Volts) at each time point. The generated laser pulses incident on a photoconductive antenna produce transient electromagnetic signals that span the THz band. Specifically, our system (TeraMatrix T-Ray 5000) covers a spectral range of over 3.5 THz and a signal-to-noise ratio above 55 dB.

By measuring the time-dependent electric field waveform rather than the time-averaged intensity of the electromagnetic wave, the transient changes due to the organic films could be obtained. Additionally, thanks to direct time-dependent sampling of the electric field, the effect of reflections due to the ion gel, substrate, or film could be removed by time-gating

the response with a Hann window, as shown in Figure S8 (Supporting Information) and as per ref. [49]. It was noted that the perturbations in the surface roughness may have caused diffusive scattering, changing the response of the THz signal. However, these perturbations were on a micron scale, and the film was illuminated with a spot size of half a centimeter at normal incidence. In this scenario, the contributions due to diffusive scattering caused by surface roughness were minimal.[50]

The system can record 100 waveforms per second where each waveform collects time samples within a time interval of 700 ps and a time resolution of 0.1 ps (corresponding to a sampling rate of 10 THz). In other words, the system has an overall measurement rate of 100 Hz. The switching speed never exceeded 5 s, which is 500 times the system's scanning rate, and thus provided an accurate measurement of their response.

For real-time modulation studies, a high signal-to-noise ratio (SNR) was achieved despite not averaging/integrating over multiple waveforms due to the dynamic range of the modulation and the time gating explained in Figure S8 (Supporting Information). This process is demonstrated for real-time modulation studies in Figure S10 (Supporting Information).

If the total power across the entire spectral range was desired, the total integrated power was measured (for each waveform) by calculating the total energy of the time domain signal (Parseval's theorem):

$$\int_{-\infty}^{\infty} \|x(t)\|^2 dt \tag{5}$$

However, since the focus is in the change in transmission across a specific spectral bandwidth, 500–900 GHz for depletion mode devices and 600–800 GHz for accumulation mode, these time domain waveforms were first converted to spectral data via Fourier transformation. Upon conversion of the time-recorded waveforms to their spectral representation, THz power was measured by integrating its power spectral density within the spectral bandwidth of interest. Formulation of this integrated power upon post-processing can be written as:

$$P = \int_{f_l}^{f_h} S(f)\, df = \int_{f_l}^{f_h} \|X(f)\|^2 df = \int_{f_l}^{f_h} \|F\{x(t)\}\|^2 df \tag{6}$$

where $S(f)$ is the power spectral density of the recorded measurement obtained after applying the Fourier transformation operation on the time data.

To obtain time-resolved modulation data, the integrated power of the spectra was measured to show the changes in transmission upon an external bias on the film. The in situ DC conductivity data were captured using a Keithley 2400 SourceMeter. A bias of ± 100 mV was applied and the resulting current was measured across the device area. This bias was repeatedly switched between the two interior contacts to avoid selective deprotonation of one side of the active region. The in situ optical transmission data were captured using a ThorLabs DET10A1 Si photodetector, with a 632 nm laser module used as a source. The UV to visible absorption data were captured separately using a Cary 5000 UV–Vis–NIR.

Supporting Information

Supporting Information is available from the Wiley Online Library or from the author.

Acknowledgements

J.S. and B.P.R. acknowledged support from the U.S. Department of Energy, Office of Basic Energy Sciences under Award #DE-SC0012458. A.K. and Y.G. acknowledged support from the National Science Foundation, grant #CNS-2145240, and the Air Force Office of Scientific Research, grant #FA9550-22-1-0382.

Conflict of Interest

The authors declare no conflict of interest.

Data Availability Statement

The data that support the findings of this study are available from the corresponding author upon reasonable request.

Keywords

electrochromic, functional, modulators, OECT, THz

Received: October 16, 2024
Revised: January 9, 2025
Published online: February 7, 2025

[1] Z. T. Ma, Z. X. Geng, Z. Y. Fan, J. Liu, H. D. Chen, *Research* **2019**, *2019*, 6482975.
[2] M. Liu, H. Y. Hwang, H. Tao, A. C. Strikwerda, K. Fan, G. R. Keiser, A. J. Sternbach, K. G. West, S. Kittiwatanakul, J. Lu, S. A. Wolf, F. G. Omenetto, X. Zhang, K. A. Nelson, R. D. Averitt, *Nature* **2012**, *487*, 345.
[3] X. Liu, B. Zhang, G. Wang, W. Wang, H. Ji, J. Shen, *Opt. Mater.* **2017**, *73*, 718.
[4] E. Kaya, N. Kakenov, H. Altan, C. Kocabas, O. Esenturk, *J. Infrared Millim. Terahertz Waves* **2018**, *39*, 483.
[5] G. Liang, X. Hu, X. Yu, Y. Shen, L. H. Li, A. G. Davies, E. H. Linfield, H. K. Liang, Y. Zhang, S. F. Yu, Q. J. Wang, *ACS Photonics* **2015**, *2*, 1559.
[6] T. Kleine-Ostmann, P. Dawson, K. Pierz, G. Hein, M. Koch, *Appl. Phys. Lett.* **2004**, *84*, 3555.
[7] B. P. Rand, H. Richter, *Organic Solar Cells: Fundamentals, Devices, and Upscaling*, CRC Press, Boca Raton, FL, USA **2014**.
[8] B. Geffroy, P. le Roy, C. Prat, *Polym. Int.* **2006**, *55*, 572.
[9] J. T. Friedlein, R. R. McLeod, J. Rivnay, *Org. Electron.* **2018**, *63*, 398.
[10] D. Ohayon, V. Druet, S. Inal, *Chem. Soc. Rev.* **2023**, *3*, 1001.
[11] J. Rivnay, S. Inal, A. Salleo, R. M. Owens, M. Berggren, G. G. Malliaras, *Nat. Rev. Mater.* **2018**, *3*, 17086.
[12] A. Nawaz, Q. Liu, W. L. Leong, K. E. Fairfull-Smith, P. Sonar, *Adv. Mater.* **2021**, *33*, 2101874.
[13] V. N. Le, J. H. Bombile, G. S. Rupasinghe, K. N. Baustert, R. Li, I. P. Maria, M. Shahi, P. A. Espejo, I. McCulloch, K. R. Graham, C. Risko, A. F. Paterson, *Adv. Sci.* **2023**, *10*, 2207694.
[14] G. Bonacchini, F. G. Omenetto, *Nat. Electron.* **2021**, *4*, 424.
[15] C. Kuang, S. Chen, M. Luo, Q. Zhang, X. Sun, S. Han, Q. Wang, V. Stanishev, V. Darakchieva, R. Crispin, M. Fahlman, D. Zhao, Q. Wen, M. P. Jonsson, *Adv. Sci.* **2023**, *11*, 2305898.
[16] C. Bortolotti, F. Grandi, M. Butti, L. Gatto, F. Modena, C. Kousseff, I. McCulloch, C. Vozzi, M. Caironi, E. Cinquanta, G. Bonacchini, *Nat. Commun.* **2024**, *15*, 9639.
[17] C. G. Tang, R. Wu, Y. Chen, Z. Zhou, Q. He, T. Li, X. Wu, K. Hou, C. J. Kousseff, I. McCulloch, W. L. Leong, *Adv. Mater.* **2024**, *36*, 2405556.
[18] Y. Zhong, N. Lopez-Larrea, M. Alvarez-Tirado, N. Casado, A. Koklu, A. Marks, M. Moser, I. McCulloch, D. Mecerreyes, S. Inal, *Chem. Mater.* **2024**, *36*, 1841.
[19] Y. Zhong, P. D. Nayak, S. Wustoni, J. Surgailis, J. Z. Parrado Agudelo, A. Marks, I. McCulloch, S. Inal, *ACS Appl. Mater. Interfaces* **2023**, *16*, 61457.
[20] M. Do, C. Park, S. Bae, J. Kim, J. H. Kim, *Org. Electron.* **2021**, *93*, 106106.
[21] R. Singh, J. Tharion, S. Murugan, A. Kumar, *ACS Appl. Mater. Interfaces* **2017**, *9*, 19427.

[22] Y. Ding, M. A. Invernale, G. A. Sotzing, *ACS Appl. Mater. Interfaces* **2010**, *2*, 1588.
[23] R. K. Hallani, B. D. Paulsen, A. J. Petty, R. Sheelamanthula, M. Moser, K. J. Thorley, W. Sohn, R. B. Rashid, A. Savva, S. Moro, J. P. Parker, O. Drury, M. Alsufyani, M. Neophytou, J. Kosco, S. Inal, G. Costantini, J. Rivnay, I. McCulloch, *J. Am. Chem. Soc.* **2021**, *143*, 11007.
[24] M. Moser, T. C. Hidalgo, J. Surgailis, J. Gladisch, S. Ghosh, R. Sheelamanthula, Q. Thiburce, A. Giovannitti, A. Salleo, N. Gasparini, A. Wadsworth, I. Zozoulenko, M. Berggren, E. Stavrinidou, S. Inal, I. McCulloch, *Adv. Mater.* **2020**, *32*, 2002748.
[25] Z. Wang, R. Liu, *Mater. Today Electron.* **2023**, *4*, 100036.
[26] J. Kawahara, P. A. Ersman, I. Engquist, M. Berggren, *Org. Electron.* **2012**, *13*, 469.
[27] G. Rebetez, O. Bardagot, J. Affolter, J. Réhault, N. Banerji, *Adv. Funct. Mater.* **2022**, *32*, 2105821.
[28] M. Moser, J. F. Ponder Jr., A. Wadsworth, A. Giovannitti, I. McCulloch, *Adv. Funct. Mater.* **2019**, *29*, 1807033.
[29] J. Luo, D. Billep, T. Waechtler, T. Otto, M. Toader, O. Gordan, E. Sheremet, J. Martin, M. Hietschold, D. R. T. Zahn, T. Gessner, *J. Mater. Chem. A* **2013**, *1*, 7576.
[30] A. K. Sarker, J. Kim, B. H. Wee, H. J. Song, Y. Lee, J. D. Hong, C. Lee, *RSC Adv.* **2015**, *5*, 52019.
[31] A. M. Ulatowski, L. M. Herz, M. B. Johnston, *J. Infrared Millim. Terahertz Waves* **2020**, *41*, 1431.
[32] J. Lloyd-Hughes, T. I. Jeon, *J. Infrared Millim. Terahertz Waves* **2012**, *33*, 871.
[33] I. Lee, G. W. Kim, M. Yang, T. S. Kim, *ACS Appl. Mater. Interfaces* **2016**, *8*, 302.
[34] L. V. Lingstedt, M. Ghittorelli, H. Lu, D. A. Koutsouras, T. Marszalek, F. Torricelli, N. I. Crăciun, P. Gkoupidenis, P. W. M. Blom, *Adv. Electron. Mater.* **2019**, *5*, 1800804.
[35] J. Rivnay, S. Inal, B. A. Collins, M. Sessolo, E. Stavrinidou, X. Strakosas, C. Tassone, D. M. Delongchamp, G. G. Malliaras, *Nat. Commun.* **2016**, *7*, 11287.
[36] S. M. Kim, C. H. Kim, Y. Kim, N. Kim, W. J. Lee, E. H. Lee, D. Kim, S. Park, K. Lee, J. Rivnay, M. H. Yoon, *Nat. Commun.* **2018**, *9*, 3858.
[37] A. Giovannitti, D. T. Sbircea, S. Inal, C. B. Nielsen, E. Bandiello, D. A. Hanifi, M. Sessolo, G. G. Malliaras, I. McCulloch, J. Rivnay, *Proc. Natl. Acad. Sci. USA* **2016**, *113*, 12017.
[38] G. Baschek, G. Hartwig, F. Zahradnik, *Polymer* **1999**, *40*, 3433.
[39] X. Li, N. T. Yardimci, D. Turan, A. Charkhesht, A. Ozcan, M. Jarrahi, *Nat. Photonics* **2024**, *18*, 139.
[40] S. Karmakar, A. Kludze, R. Chandra, Y. Ghasempour, *Nat. Food* **2025**, *6*, 97.
[41] H. Sarieddeen, N. Saeed, T. Y. Al-Naffouri, M. Alouini, *IEEE Commun. Mag.* **2020**, *58*, 69.
[42] A. Kludze, J. Kono, D. M. Mittleman, Y. Ghasempour, *Nat. Commun.* **2024**, *15*, 8756.
[43] N. Ashraf, T. Saeed, H. Taghvaee, S. Abadal, V. Vassiliou, C. Liaskos, A. Pitsillides, M. Lestas, *IEEE Trans. Intell. Transp. Syst.* **2023**, *24*, 4848.
[44] A. Giovannitti, C. B. Nielsen, D. T. Sbircea, S. Inal, M. Donahue, M. R. Niazi, D. A. Hanifi, A. Amassian, G. G. Malliaras, J. Rivnay, I. McCulloch, *Nat. Commun.* **2016**, *7*, 13066.
[45] O. Knopfmacher, M. L. Hammock, A. L. Appleton, G. Schwartz, J. Mei, T. Lei, J. Pei, Z. Bao, *Nat. Commun.* **2014**, *5*, 2954.
[46] M. Xie, H. Liu, M. Wu, C. Chen, J. Wen, L. Bai, J. Yu, W. Huang, *Org. Electron.* **2023**, *117*, 106777.
[47] K. H. Lee, M. S. Kang, S. Zhang, Y. Gu, T. P. Lodge, C. D. Frisbie, *Adv. Mater.* **2012**, *24*, 4457.
[48] D. Koutsouras, F. Torricelli, P. Gkoupidenis, P. W. M. Blom, *Adv. Mater. Technol.* **2021**, *6*, 2100732.
[49] R. Shen, Y. Ghasempour, *IEEE Trans. Commun.* **2024** 1.
[50] M. Koch, D. M. Mittleman, J. Ornik, E. Castro-Camus, *Nat. Rev. Methods Primers.* **2023**, *3*, 48.